



The microstructural basis for the mechanical properties and electrical resistivity of nanocrystalline Cu–Al₂O₃

S. Nachum^a, N.A. Fleck^{a,*}, M.F. Ashby^a, A. Colella^b, P. Matteazzi^c

^a Cambridge University, Eng. Dept., Trumpington St., Cambridge CB2 1PZ, UK

^b CSGI, Via della Lastruccia, 50019 Sesto Fiorentino, Italy

^c MBN Nanomaterialia S.p.A., Via Bortolan 42-A, 31050 Vascon di Carbonera, Italy

ARTICLE INFO

Article history:

Received 30 July 2009

Received in revised form 12 February 2010

Accepted 23 April 2010

Keywords:

Nanocrystalline alloys
Electrical resistivity
Dispersion strengthening
Shear bands
Nano-indentation

ABSTRACT

The mechanical properties and electrical resistivity of nanocrystalline copper reinforced by 1 vol.% and 5 vol.% of nano-alumina particles have been measured. The composites were prepared by ball-milling and consolidated by a combination of hot extrusion and HIPing. The uniaxial tensile and compressive strengths are comparable for each composite, and an elastic, ideally plastic response is observed. Shear bands, of width a few microns, accompany plastic deformation. A number of microstructural characterisation tools were used to reveal that grain boundary strengthening and dispersion strengthening are the dominant strengthening mechanisms. Nano-indentation measurements reveal a size effect in hardness. The electrical resistivity is almost double that of pure oxygen free copper and this is mainly ascribed to the presence of dissolved iron.

© 2010 Elsevier B.V. All rights reserved.

1. Introduction

Materials of high yield strength, hardness and high electrical conductivity are required in a number of engineering applications. Nanocrystalline copper reinforced by fine oxide particles possess these beneficial properties [1–4], exploiting both grain boundary strengthening and dispersion strengthening [5–14]. The high electrical conductivity of copper is preserved because neither the dispersion of particles nor the small grain size greatly degrade it [15]. One way of manufacturing nanocrystalline alloys with fine and stable dispersed oxide particles is by ball-milling and mechanical alloying [16]. Metal powders are mixed and milled with steel balls until a homogeneous dispersion of oxide particles is achieved and the grain size of the copper matrix is refined. This study explores the structure, the mechanical behaviour and the electrical resistivity of nanocrystalline copper reinforced by 1 vol.% and 5 vol.% of nano-alumina particles made in this way.

2. Experimental procedures

2.1. Material fabrication process

Ball-milling of powders, followed by hot extrusion and HIPing was used in order to manufacture nanocrystalline copper with a

dispersion of 1 vol.% and 5 vol.% alumina. The process steps are as follows:

- (i) Powders of 99.5% purity Cu (size range 45–350 μm), 99.4% purity Al (size range 75–350 μm) and 99.6% purity CuO (size range 45–350 μm) were ball-milled in vacuum at room temperature for 9 h using a steel container and steel balls.¹ The volume ratio of balls to powder was 15:1 and the powder size distribution after milling was below 500 μm. Two volume fractions of alumina, 1 vol.% and 5 vol.%, were formed during the high energy milling process by a redox reaction between the Al and the CuO powders, exploiting the reaction [2]: $X\text{Cu} + 3\text{CuO} + 2\text{Al} = (X+3)\text{Cu} + \text{Al}_2\text{O}_3$. The Al and CuO powders were in stoichiometric proportion in order to give Al₂O₃ particles dispersed within the Cu matrix, with no residual Al or CuO after the ball-milling operation. The reaction of Al and CuO is highly exothermic ($\Delta H = -1209$ kJ/mol) with a high reaction rate that requires only a few minutes of milling to activate and complete the reaction, see for example [17].
- (ii) Following milling, the powders were consolidated to bars of length 38 mm and diameter 16 mm by extrusion under argon at 25 MPa and 900 °C at a rate of 3 mm s⁻¹ and an extrusion ratio of 8. This was followed by HIPing² in an argon atmosphere for 30 min under a pressure of 100 MPa and at 600 °C.

* Corresponding author. Tel.: +44 01223 748240; fax: +44 01223 332662.
E-mail address: naf1@cam.ac.uk (N.A. Fleck).

¹ MBN Nanomaterialia S.p.A. Italy.

² CSGI Italy.

2.2. Microstructure characterisation

The microstructures were probed by Transmission Electron Microscopy (TEM), Scanning Electron Microscopy (SEM) and Atomic Force Microscopy (AFM), as follows:

- (i) Bright field and dark field TEM images, TEM diffraction patterns and X-ray spectroscopy mapping were each taken at 300 kV.³ The TEM samples were prepared from discs mechanically thinned to 20 μm . A droplet of 70% nitric acid and 30% purified water chemically thinned the disks to TEM foils.
- (ii) Samples for the high-resolution scanning microscope⁴ were polished using a series of polishing powders down to 0.06 μm colloidal silica and were then etched by 4% Nital solution. The samples were imaged in back-scattered and secondary electron modes and were chemically mapped using X-ray spectroscopy. Additionally, samples were probed using an X-ray diffractometer in order to determine the constituent phases.
- (iii) An AFM⁵ in contact mode was used to measure the size and shape of the copper grains. Samples were prepared in the same manner as for the SEM examination.
- (iv) The electrical resistivity of both composites was measured using a four-probe technique⁶ and also by an eddy-current technique.⁷ The two techniques gave essentially the same values for resistivity.

2.3. Mechanical tests

Micro-indentation and nano-indentation tests, and uniaxial tension and compression tests were performed on specimens machined from the HIPed bar stock. The details are as follows:

- (i) Samples for micro-hardness measurement were mechanically polished using a sequence of powders down to 0.06 μm colloidal silica. The samples for nano-indentation were similarly polished and were then electro-polished.⁸ The micro-hardness was measured with a Vickers indenter⁹ at five different loads (20 N, 10 N, 5 N, 3 N and 1 N); the hardness data reported below were the average values from 10 indentations at each load. Nano-indentation tests were performed with a Berkovich tip¹⁰ at loads between 250 μN and 10 mN. A 5 s ramp time was used for loading and unloading and the peak load was maintained for 2 s. The contact area in each indent test was determined from the unloading stiffness, as suggested by Oliver and Pharr [18].
- (ii) Uniaxial tension and compression tests were performed at a quasi-static strain rate of 10^{-3} s^{-1} ; in all tests the loading direction was aligned with the extrusion direction. The compression tests were performed on cylindrical specimens, of diameter 3 mm and length 5 mm; the samples were compressed between hardened, polished steel platens lubricated with petroleum jelly. In the tensile tests, dog-bone specimens were used, of 3 mm \times 3 mm square cross-section and of gauge length 8 mm; this shape was used in order to facilitate the observation of shear bands. The surfaces of the dog-bone specimens were polished to a mirror finish using 0.06 μm colloidal silica. In order to highlight the size and orientation of the shear bands,

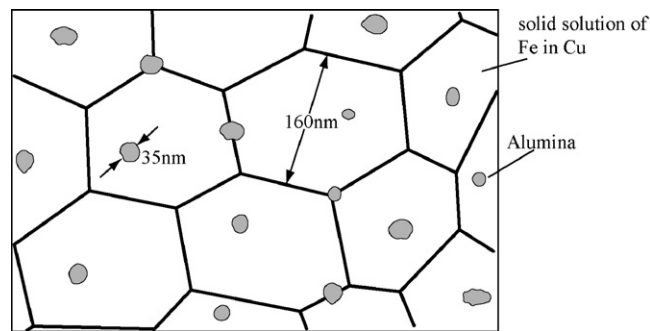


Fig. 1. A sketch of the microstructure.

final polishing was performed along the direction of loading; consequently, the as-prepared specimens contained a set of light scratches along the axial direction. The tensile (and compression) samples were loaded in a uniaxial, screw-driven test machine; the axial strain was measured using a resistance strain gauge at strain levels below 2% and using a laser gauge at higher levels of strain.

3. Experimental results

3.1. The observed microstructure

Before detailing the results from each characterisation technique, it is instructive to summarise the observed microstructure of both composites, see the sketch in Fig. 1. Discrete particles of alumina of diameter approximately 35 nm are dispersed within Cu grains of diameter 160 nm; the spacing but not diameter of the alumina particles is dependent upon the volume fraction of alumina phase. Additionally, about 0.1 wt.% Fe, picked up during ball-milling, is dissolved within the Cu grains. There is no evidence for porosity in either composite: the measured densities are in excellent agreement with the theoretical values for full density. The characterisation techniques detailed above gave the following results.

³ Philips CM30.

⁴ JEOL 6340F FEGSEM.

⁵ Veeco CP-II.

⁶ An HP(6612C) digital multimeter.

⁷ Hocking Autosigma2000 near-surface eddy current instrument with a 6 mm probe.

⁸ Struers ElectroPol-5 filled with electrolyte D2.

⁹ Shimadzu HMV.

¹⁰ Hysitron Ubi1.

- (i) The X-ray diffraction measurements showed strong peaks for Cu and a much smaller peak for alumina. Diffractions from free Al or other phases such as the oxide phases CuAl_2O_4 , CuAlO_2 , Cu_2O , CuO , FeO , Fe_2O_3 and Fe_3O_4 were absent. This implies that the dominant phases are Cu and alumina.
- (ii) Back-scattered SEM micrographs taken from the 1 vol.% and the 5 vol.% composite are given in Fig. 2(a) and (b), respectively. The grey domains are the Cu grains, whereas the black particles are Al_2O_3 of mean diameter 35 nm.
- (iii) Bright and dark field TEM images, diffraction patterns and X-ray spectroscopy mapping have all been employed for both composites. A typical TEM image is given in Fig. 3(a) and the corresponding diffraction pattern is shown in Fig. 3(b) for the 5 vol.% composite; the equivalent images for the 1 vol.% are omitted for the sake of brevity. For both composites, the Cu grain size is 170 nm and alumina particles, of average diameter 40 nm, are located both within the Cu matrix and at Cu grain boundaries. The diffraction rings correspond to copper and alumina phases. X-ray spectroscopy mapping confirmed the presence of Al and O in the stoichiometric proportion of Al_2O_3 [3].
- (iv) Topographic images taken by an AFM in contact mode suggested that the Cu grains are equiaxed and of average diameter 160 nm for both compositions of composite. A typical image of the etched surface of the 1 vol.% composite is shown in Fig. 4.

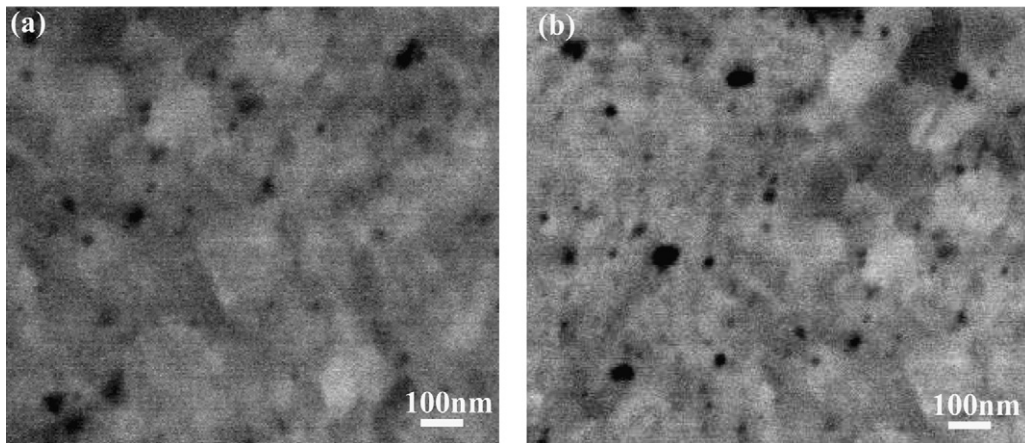


Fig. 2. SEM micrographs of (a) 1 vol.% and (b) 5 vol.% composites.

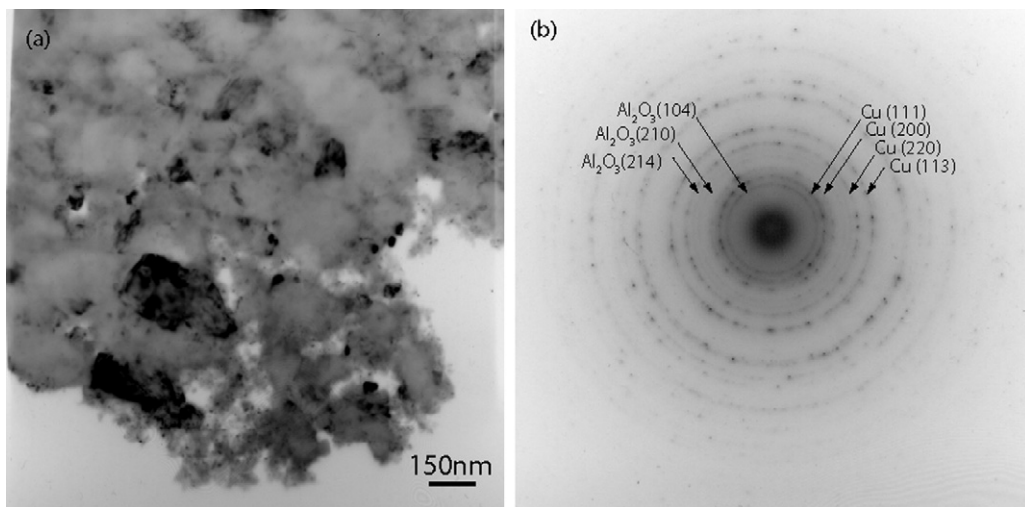


Fig. 3. (a) Dark field and (b) diffraction pattern images from the 5 vol.% composite.

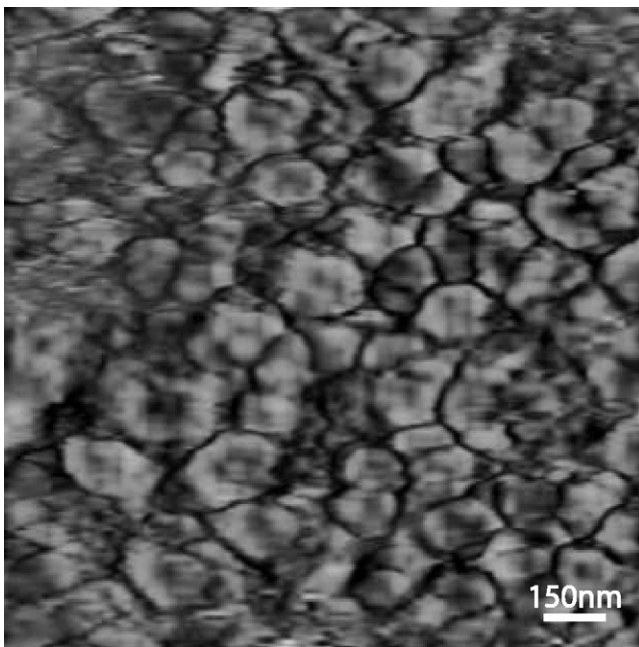


Fig. 4. AFM topography image of the 1 vol.% composite, taken in the contact mode.

3.2. Electrical resistivity

It is well-known that a small volume fraction of dissolved species can lead to a major increase in electrical resistivity. For the composites under consideration, there is a small but unknown volume fraction of dissolved Fe within the Cu. We now make use of electrical resistivity measurement in order to deduce the volume fraction of dissolved Fe.

The electrical resistivity of pure Cu is $\rho_0 = 16.7 \text{ n}\Omega \text{ m}$ [19]. The measured resistivity of the 1 vol.% composite was $34 \pm 1 \text{ n}\Omega \text{ m}$, twice that for pure copper. For the 5 vol.% composite, the electrical resistivity rises slightly more to $39 \pm 1 \text{ n}\Omega \text{ m}$. The large increase in electrical resistivity for the composites compared to the pure Cu is mainly attributed to the presence of dissolved Fe within the Cu for the following reasons:

- (i) The Cu matrix is in an annealed state following the extrusion and HIPing operations. Consequently, the mean dislocation density is comparable to that of pure Cu in the annealed state, and this is not the underlying cause of the resistivity enhancement.
- (ii) The presence of Cu grain boundaries increases the electrical resistivity according to Ref. [15]:

$$\Delta\rho_G = \frac{2}{3} \rho_{gb} \left(\frac{S}{V} \right) \quad (1)$$

Table 1
The main mechanical properties of the 1 vol.% and 5 vol.% composites.

Vol. fraction alumina (%)	Young's modulus E (GPa)	0.2% offset tensile yield strength σ_Y (MPa)	UTS (MPa)	Ductility $\varepsilon\%$	H_0 (GPa)
1	119	460	520	10	1.4
5	120	620	775	11	2.35

where ρ_{gb} is the specific grain boundary resistivity and for Cu $\rho_{gb} = 3.12 \times 10^{-16} \Omega \text{ m}$ [15]. The ratio S/V is the grain boundary surface area S per unit volume V . This ratio can be approximated to be $2.37/d_G$ [15], where d_G is the Cu grain size assuming the shape of a tetrakaidecahedron. Upon substituting values, the presence of grain boundaries enhances the electrical resistivity by $\Delta\rho_G = 5\text{--}2.5 \text{ n}\Omega \text{ m}$ for Cu grain sizes in the range of 100–200 nm, respectively.

- (iii) The enhancement in electrical resistivity due to a volume fraction f of alumina particles is [20]:

$$\Delta\rho_P = \rho_m \frac{3f}{2(1-f)} \quad (2)$$

where

$$\rho_m = \rho_0 + \Delta\rho_G \quad (3)$$

We thereby estimate $\Delta\rho_G = 0.33 \text{ n}\Omega \text{ m}$ and $1.76 \text{ n}\Omega \text{ m}$ for 1 vol.% and 5 vol.% of alumina, respectively.

- (iv) The contributions to resistivity from the alumina particles and the Cu grain boundaries sum to about $5 \text{ n}\Omega \text{ m}$, while the observed enhancement is approximately $20 \text{ n}\Omega \text{ m}$ for both composites. The presence of a solid solution considerably alters the mean free path of electrons. Consequently, the electrical resistivity changes linearly with the atomic concentration of the solid solution according to Ref. [21]:

$$\Delta\rho_S = \beta c \quad (4)$$

where c is the weight percentage of solid solution and the coefficient β is the change in electrical resistivity for 1 wt.% of solid solution. For a solid solution of Fe in Cu, β equals $115 \text{ n}\Omega \text{ m (wt.\%)}^{-1}$ [22], and so a solid solution of 0.13 wt.% will give the required increase in resistivity by $15 \text{ n}\Omega \text{ m}$. This concentration of solid solution is plausible: the Cu–Fe phase diagram [23] shows that up to 2 wt.% Fe is soluble in Cu at 900°C .

In contrast, β equals only to $12.8 \text{ n}\Omega \text{ m (wt.\%)}^{-1}$ for Al dissolved in Cu [22]. For the 1 vol.% Al_2O_3 composite only 0.24 wt.% Al was present in the pre-mixed powder. It is argued above that all of the Al reacts with the CuO. Had none of the Al reacted and had instead gone into solid solution in the Cu, then the increase in electrical resistivity would be $3 \text{ n}\Omega \text{ m}$. This is much less than the observed increase of $15 \text{ n}\Omega \text{ m}$ for both composites.

The Al powder contains 0.4 wt.% Fe and 0.3 wt.% Si. Consequently, the composite contains $9.6 \times 10^{-4} \text{ wt.\% Fe}$ and $7.2 \times 10^{-4} \text{ wt.\% Si}$. The increase in electrical resistivity from the Fe and from the Si would be $0.11 \text{ n}\Omega \text{ m}$ and $0.0036 \text{ n}\Omega \text{ m}$ [22], respectively. These values are more than two orders of magnitude less than the observed increase of $15 \text{ n}\Omega \text{ m}$. Thus, the increase in resistivity cannot be traced to the impurities within the Al powder. The Cu powder contains 0.4 wt.% CuO as an impurity. This oxide is converted to Al_2O_3 during the ball-milling operation. It is therefore argued that the increase in electrical resistivity is due to the pick-up of Fe from the ball-milling operation. This observation of Fe pick-up during ball-milling has been previously noted, see for example [12].

- (v) Negligible porosity was present in the samples: density measurements and microscopic observations confirmed that the level of porosity following the HIP operation is below 0.1 vol.%. The enhancement in electrical resistivity due to 0.1 vol.% of voids is comparable to that induced by about 0.1 vol.% of insu-

lating Al_2O_3 particles, and is of magnitude $0.05 \text{ n}\Omega \text{ m}$ [20]. We conclude that the increase in electrical resistivity is not due to porosity.

3.3. Mechanical properties

3.3.1. The tensile and compressive responses

The true stress versus logarithmic strain responses in uniaxial tension and compression are shown in Fig. 5 for both composites. The responses can be described as elastic, ideally plastic for both composites, and there is a negligible difference between the tensile and compressive behaviours. The 1 vol.% and 5 vol.% composites have UTS values of 520 MPa and 775 MPa, respectively, and both display an elongation to failure in tension of 10%. Table 1 summarises the mechanical properties of the two composites.

An examination of the tensile fracture surfaces in the SEM revealed that failure was by microvoid coalescence, with the voids initiating at the weak copper–alumina interfaces, see Fig. 6. The final void spacing was comparable to the spacing between the alumina particles, and no pre-existing porosity was observed. On the macroscopic level, a cup-and-cone neck was observed.

Plastic deformation was by multiple shear bands in both the tensile and the compressive tests. The nature of the shear bands was explored in selected tension tests by interrupting the test and directly observing the shear bands at the surface of the highly polished specimen. These tensile specimens were successively strained in increments of 0.5% plastic strain and were then unloaded. The gauge section was examined using an optical microscope and an SEM; a typical SEM micrograph is shown in Fig. 7. The image reveals numerous shear bands, each of width a few microns and oriented at 49° to the loading direction. With progressive macroscopic straining, material within each band strain hardens and this leads to broadening of the band. Shear bands of this type have been observed previously in nanocrystalline Fe (bcc) and Cu (fcc) [10–14]; such shear bands are characteristic of alloys of high strength and low strain hardening capacity.

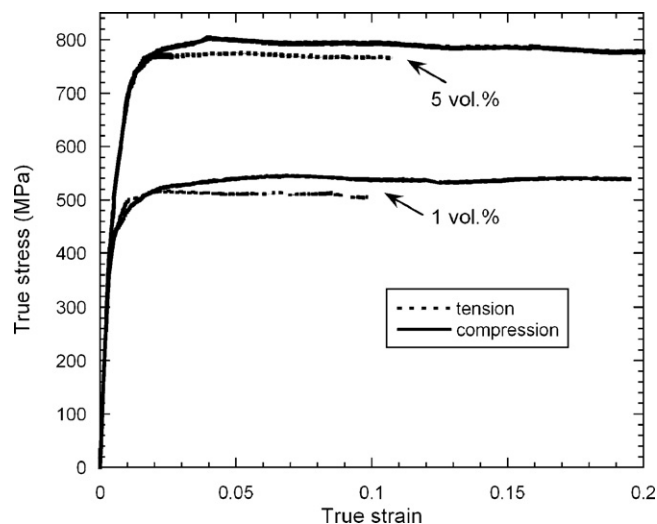


Fig. 5. True stress versus true (logarithmic) strain uniaxial responses for the 1 vol.% and 5 vol.% composites.

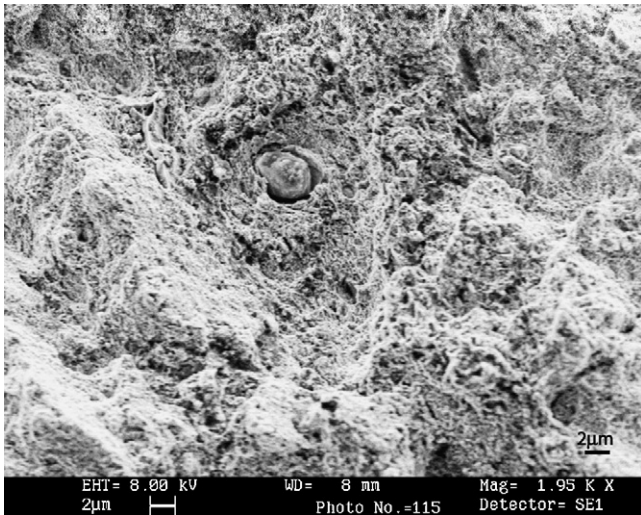


Fig. 6. SEM micrograph of the tensile fracture surface in the cup region of the 5 vol.% composite.

3.4. Hardness tests

Fig. 8 shows the hardness H as a function of contact depth h for both composites. A pronounced size effect is observed, such that the observed hardness almost doubles when the contact depth is reduced from 1 μm to 0.1 μm . Such size effects have been observed previously in a wide range of alloys [24–32].

At large indent depths (above 5 μm) the hardness is almost constant at 1.4 GPa and 2.35 GPa for the 1 vol.% and 5 vol.% composites, respectively. Recall that the Vickers hardness of a large indent is approximately three times the flow strength in uniaxial tension at a representative plastic strain of 8%, see Tabor [33]. Upon substituting values we find $H/\sigma_{\text{UTS}} \approx 2.7$ and 3.0 for the 1 vol.% and 5 vol.% composites, respectively.

4. Discussion

4.1. Strengthening mechanisms

Recall that the yield strength is 460 MPa and 620 MPa for the 1 vol.% and 5 vol.% composites, respectively. These values are much higher than the typical yield strength of 45–55 MPa for annealed copper of grain size 100 μm . What are the reasons for the strength elevation? We shall now argue that the strength is enhanced mainly by grain boundary strengthening and dispersion strengthening, and to a much lesser degree by solute strengthening.

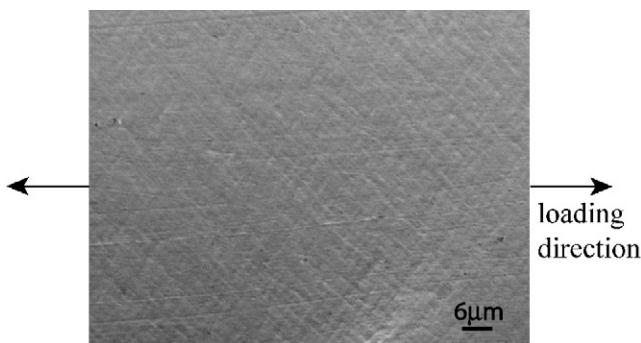


Fig. 7. SEM micrograph from the 1 vol.% composite at a tensile strain of ~3.5%. The image reveals numerous shear bands a few microns in width oriented at ~49° to the loading direction.

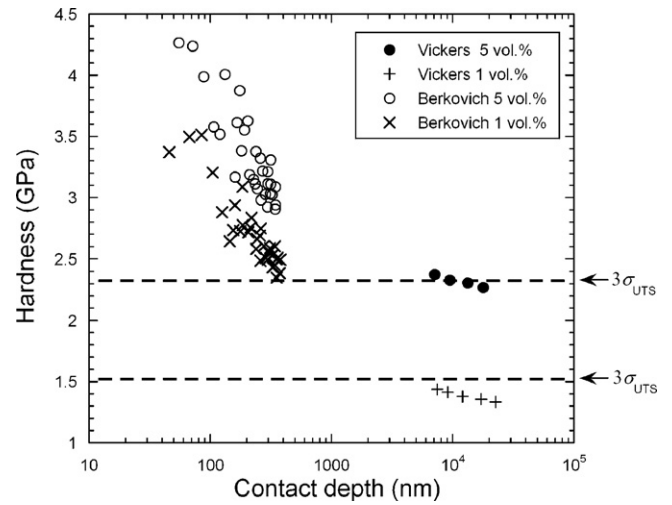


Fig. 8. Hardness versus contact depth for the 1 vol.% and 5 vol.% composites.

These three strengthening mechanisms are modelled, respectively, by the Hall–Petch relation, the Orowan mechanism and dislocation–solute interactions [34,35].

- (i) The Hall–Petch relation of grain boundary strengthening predicts that the yield strength elevation $\Delta\sigma_G$ scales with the copper grain size d_G according to Ref. [34]:

$$\Delta\sigma_G = \frac{K_{\text{HP}}}{\sqrt{d_G}} \tag{5}$$

where $K_{\text{HP}} = 0.142 \text{ MPa m}^{1/2}$ for copper [36]. Upon noting that $d_G = 160 \text{ nm}$ for both the 1 vol.% and 5 vol.% composites, we obtain $\Delta\sigma_G = 381 \text{ MPa}$. This is a major contribution to strength. The potency of grain boundary strengthening in nanocrystalline copper has been previously noted, see [5,9,11,12]. The strength contribution as noted in these studies is plotted as a function of $(d_G)^{-1/2}$ in Fig. 9, and good agreement with Eq. (5) is noted.

- (ii) The Orowan mechanism gives the elevation in yield strength $\Delta\sigma_P$ due to the bowing of dislocations between neighbouring

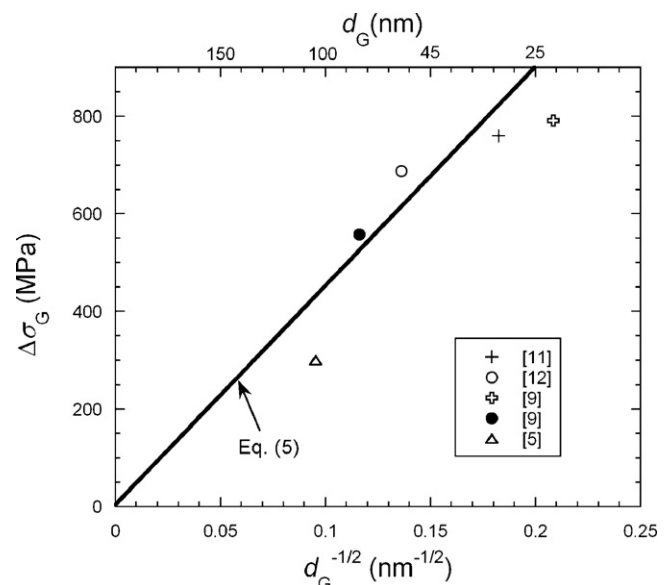


Fig. 9. The effect of Cu grain size upon the yield strength of nanocrystalline copper. The solid line is the Hall–Petch relation (5).

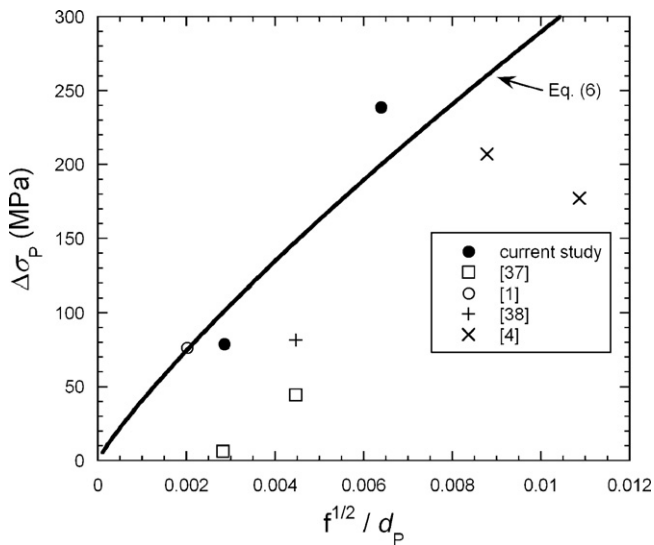


Fig. 10. The effect of volume fraction and size of the alumina particles upon the strength of nanocrystalline copper reinforced by alumina particles.

hard particles. In the present case, the hard particles are alumina of diameter $d_p = 35$ nm, and of volume fraction $f = 0.01$ and 0.05 . The elevation in strength $\Delta\sigma_p$ also depends upon the shear modulus G and the Burgers vector b according to Ref. [35]:

$$\Delta\sigma_p = \frac{1}{2\pi} \frac{Gmb\sqrt{f}}{d_p} \ln\left(\frac{d_p}{b} \sqrt{\frac{\pi}{6f}}\right) \quad (6)$$

where the Taylor factor is $M = 3$ [35]. For Cu, we take $G = 42$ GPa and $b = 0.256$ nm, giving $\Delta\sigma_p = 101$ MPa and 200 MPa for the 1 vol.% and 5 vol.% composites, respectively. The ability of alumina particles to give dispersion strengthening in nanocrystalline copper has already been documented [1,4,37,38]. Upon subtracting off the Hall–Petch contribution (using Eq. (5)) and the Peierls stress of order (4 MPa [39]), the contribution from dispersion strengthening is plotted in Fig. 10 as a function of $f^{1/2}/d_p$. Relation (6) approximately describes the effect of dispersion strengthening in these alloys.

(iii) Solid solution strengthening is based upon dislocation–solute interactions and is given by [34]:

$$\Delta\sigma_s = \frac{\sqrt{3}G\varepsilon_s^{3/2}c^{1/2}}{700} \quad (7)$$

for a solid of shear modulus G , solute concentration c and interaction parameter ε_s . For Fe dissolved in Cu we have $\varepsilon_s = 1.5$ [40]. The electrical resistivity measurements suggest that the mass fraction of Fe dissolved in Cu is $c = 0.1$ wt.% for both composites. Consequently, the contribution of solid solution strengthening to the yield strength for both composites is 6 MPa. This contribution is much less than that of grain boundary strengthening and dispersion strengthening.

The relative contributions from the three strengthening mechanisms is summarised in Fig. 11. Upon summing the strength contributions, good agreement is found with the measured yield strengths. We conclude that grain boundary strengthening is the dominant contribution to the yield strength in both composites.

4.2. Nano-indentation

Micro- and nano-indentation experiments on metals show size effects in hardness for indent depths below a few microns [24–30]: the hardness increases with diminishing depth. A relation between

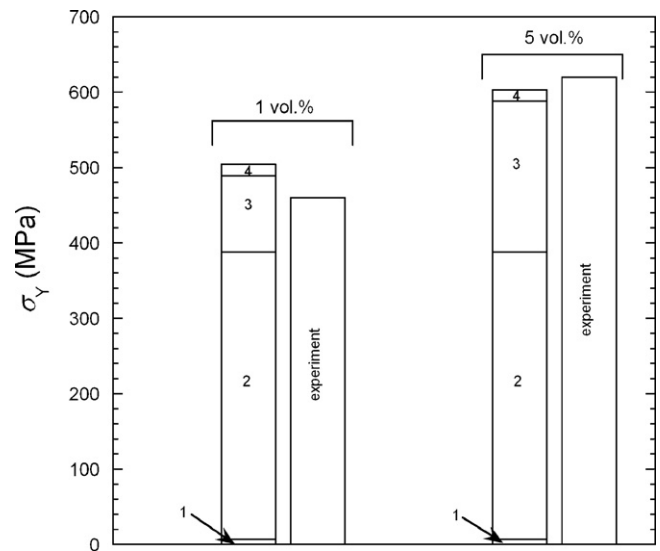


Fig. 11. Summation of the strengthening contributions and comparison with measured yield strength σ_y for both composites, where (1) Peierls stress, (2) grain boundary strengthening, (3) dispersion strengthening and (4) solid solution strengthening.

the hardness (H) and the indentation depth (h) has been established by the theoretical analysis of Poole et al. [24] (and subsequently elaborated upon by Nix and Gao [26]):

$$\left(\frac{H}{H_0}\right)^2 = 1 + \frac{h^*}{h} \quad (8)$$

where h^* is a material length scale and H_0 is the hardness at large indentation depths ($h \gg h^*$). This model is based upon the notion that plastic strain gradients induce geometrically necessary dislocations and thereby elevate strength. The hardness data of Fig. 8 have been re-plotted in Fig. 12 in the form of $(H/H_0)^2$ versus $1/h$: the data for both composites support the prediction (8), and give the values $h^* = 0.45 \mu\text{m}$ and $0.25 \mu\text{m}$ for the 1 vol.% and 5 vol.% composites, respectively. For indentations depths larger than 200 nm the former and the later lines are the best fit to the 1 vol.% and 5 vol.%

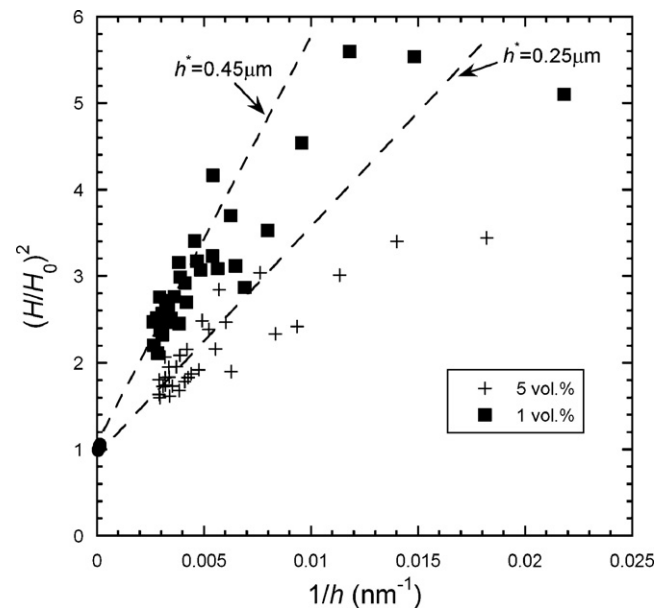


Fig. 12. Indentation data for the 1 vol.% and 5 vol.% composites, re-plotted in order to determine the accuracy of the prediction (8).

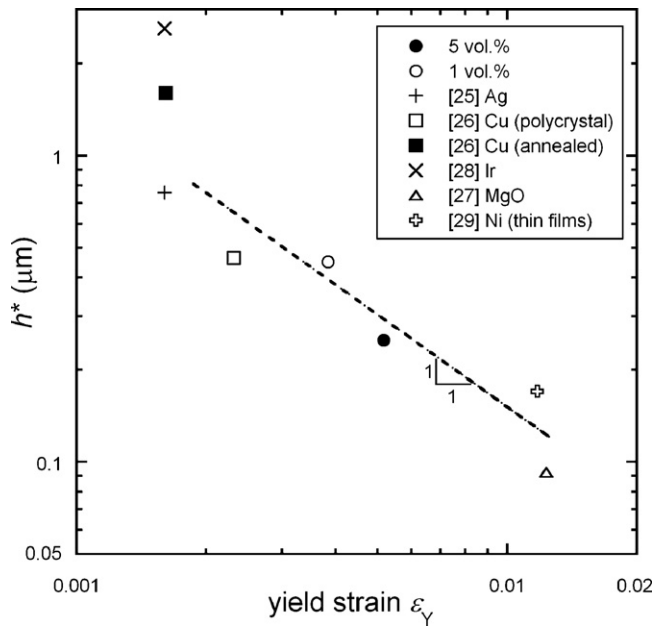


Fig. 13. The relation between material length scale h^* and the tensile yield strain ε_Y .

composite data, respectively. The data for depths below 200 nm deviate from the linear relation of Eq. (8). It has already been noted [27–30] that the linear relation between $(H/H_0)^2$ and $1/h$ is obeyed for indentation depths above 100 nm, and at smaller depths the linear relation over-estimates the hardness.

Following [31], it is instructive to explore the dependence of h^* upon the uniaxial yield strain ε_Y for a range of alloys, and from single crystals to nanocrystals. Data from the present study, along with data taken from the literature [25–29] for a wide range of metals, are plotted in the form of h^* versus ε_Y , see Fig. 13. A clear trend emerges such that h^* scales approximately with $1/\varepsilon_Y$. This is consistent with the following simple argument. Assume that the internal material length scale in strain gradient theory [24,26,32] is of order h^* and identify it with the length scale governing dislocation motion. Then recall the Orowan relation, and re-express it in the form:

$$\sigma_Y \approx \frac{Eb}{h^*} \quad (9)$$

Consequently, we find $h^* \approx b/\varepsilon_Y$ and this is consistent with the trend given in Fig. 13.

5. Conclusions

This study examines the uniaxial mechanical properties and the electrical resistivity of nanocrystalline Cu reinforced by 1 vol.% and 5 vol.% nano-alumina particles. The composites were made by reactive mechanical alloying powders followed by a consolidation of hot extrusion and HIPing, and the following conclusions are drawn.

- (i) A copper grain size of 160 nm is observed, reinforced with alumina particles of diameter 35 nm. Electrical resistivity measurements suggest that 0.1 wt.% of Fe is dissolved within the copper matrix during the powder consolidation process.

- (ii) Both composites have a high tensile strength with minimal strain hardening, and display a ductility of 10%; also, the uniaxial responses are symmetrical in tension and in compression. Shear bands of width a few microns accompany plastic deformation. The dominant strengthening mechanisms are grain boundary strengthening and dispersion strengthening.
- (iii) Nano-indentation tests show a pronounced size effect: hardness increases with diminishing indentation depth. The Nix–Gao linear relation between $(H/H_0)^2$ and $1/h$ is observed over a restricted range of indent depths.

Acknowledgments

The authors are grateful for financial support from the Framework Programme FP6, Contract No. NMP2-CT-2006-026467 “Manudirect: Ultraprecision direct manufacturing”.

References

- [1] T. Baohong, et al., *Mater. Sci. Eng. A* 435–436 (2006) 705–710.
- [2] T. Venugopal, K. Prasad Rao, B.S. Murty, *Mater. Sci. Eng. A* 393 (2005) 382–386.
- [3] P.K. Jena, E.A. Brocchi, I.G. Solórzano, M.S. Motta, *Mater. Sci. Eng. A* 371 (2004) 72–78.
- [4] D.V. Kudashov, et al., *Mater. Sci. Eng. A* 387–389 (2004) 768–771.
- [5] P.G. Sanders, et al., *Acta Mater.* 45 (1997) 4019–4025.
- [6] D. Jia, K.T. Ramesh, E. Ma, *Acta Mater.* 51 (2003) 3495–3509.
- [7] M.A. Meyers, A. Mishra, D.J. Benson, *Prog. Mater. Sci.* 51 (2006) 427–556.
- [8] Y. Wang, M. Chen, F. Zhou, E. Ma, *Nature* 419 (2002) 912–915.
- [9] K. Ramesh, et al., *Mater. Sci. Eng. A* 463 (2007) 14–21.
- [10] D. Jia, K.T. Ramesh, E. Ma, *Scripta Mater.* 42 (2000) 73–78.
- [11] Y.M. Wang, K. Wang, D. Pan, K. Lu, K.J. Hemker, E. Ma, *Scripta Mater.* 48 (2003) 1581–1586.
- [12] S. Cheng, E. Ma, Y.M. Wang, L.J. Kecskes, K.M. Youssef, C.C. Koch, U.P. Trociewitz, K. Han, *Acta Mater.* 53 (2005) 1521–1533.
- [13] Q. Wei, L. Kecskes, T. Jiao, K.T. Hartwig, K.T. Ramesh, E. Ma, *Acta Mater.* 52 (2004) 1859–1869.
- [14] Q. Wei, D. Jia, K.T. Ramesh, E. Ma, *Appl. Phys. Lett.* 81 (2002) 1240–1242.
- [15] E. Botcharova, J. Freudenberger, L. Schultz, *Acta Mater.* 54 (2006) 3333–3341.
- [16] C. Suryanarayana, *Prog. Mater. Sci.* 46 (2001) 1–184.
- [17] D.L. Zhang, J.J. Richmond, *J. Mater. Sci.* 34 (1999) 701–706.
- [18] W.C. Oliver, G.M. Pharr, *J. Mater. Res.* 7 (1992) 1564–1583.
- [19] *ASM Handbook, Properties & Selection: Nonferrous Alloys and Special-purpose Materials*, vol. 3, ASM International, 2002.
- [20] P.S. Phani, V. Vishnukanthan, G. Sundararajan, *Acta Mater.* 55 (2007) 4741–4751.
- [21] P.L. Rossiter, *The Electrical Resistivity of Metals and Alloys*, Cambridge University Press, Cambridge, UK, 1987.
- [22] H. Pops, *IEEE Elec. Insul. Mag.* 11 (5) (1995) 17–23.
- [23] *ASM Handbook, Alloy Phase Diagrams*, vol. 3, ASM International, 2002.
- [24] W.J. Poole, M.F. Ashby, N.A. Fleck, *Scripta Mater.* 34 (4) (1996) 559–564.
- [25] Q. Ma, D.R. Clarke, *J. Mater. Res.* 10 (4) (1995) 583–586.
- [26] W.D. Nix, H.J. Gao, *J. Mech. Phys. Solids* 46 (3) (1998) 411–425.
- [27] G. Feng, W.D. Nix, *Scripta Mater.* 51 (2004) 599–603.
- [28] J.G. Swadener, et al., *J. Mech. Phys. Solids* 50 (2002) 681–694.
- [29] M. Zengsheng, et al., *J. Appl. Phys.* 103 (2008) 043512.
- [30] Y. Huang, F. Zhang, K.C. Hwang, W.D. Nix, G.M. Pharr, G. Feng, *J. Mech. Phys. Solids* 54 (2006) 1668–1686.
- [31] A.G. Evans, J.W. Hutchinson, *Acta Mater.* 57 (2009) 1675–1688.
- [32] N.A. Fleck, J.W. Hutchinson, *J. Mech. Phys. Solids* 49 (2001) 2245–2271.
- [33] D. Tabor, *The Hardness of Metals*, Oxford University Press, New York, 1951.
- [34] T.H. Courtney, *Mechanical Behavior of Materials*, McGraw-Hill Inc., Singapore, 1990.
- [35] D. Preininger, *J. Nucl. Mater.* 329–333 (2004) 362–368.
- [36] D.J. Benson, H.H. Fu, M.A. Meyers, *Mater. Sci. Eng. A* 319–321 (2001) 854–861.
- [37] R.H. Palma, A.Q. Sepulveda, *Third International Latin-American Conference on Powder Technology*, Florianopolis, Brazil, November 26–28, 2001.
- [38] R.K. Islamgaliev, et al., *Mater. Sci. Eng. A* 319–321 (2001) 872–876.
- [39] R. Wang, Q.F. Fang, *J. Alloys Compd.* 310 (2000) 80–84.
- [40] H. Wendt, R. Wagner, *Acta Metall.* 30 (1982) 1561–1570.